

# Uncovering the Fourier Structure of Wavefunctions in Semiconductors

Yunfan Liang,<sup>1</sup> Damien West,<sup>1</sup> and Shengbai Zhang<sup>1</sup>

<sup>1</sup>*Department of Physics, Applied Physics and Astronomy,  
Rensselaer Polytechnic Institute, Troy, NY, 12180, USA*

(Dated: August 18, 2025)

Symmetry dictates the physical properties of materials. The symmetry of the Bravais lattice defines the set of points, lines, and planes over which sets of planewaves are degenerate, upon which atomic symmetry determines the interaction potentials which may lift such degeneracies. This results in wavefunctions which are single planewaves throughout the BZ, except in the vicinity of the removed degeneracies. As optical transitions between any two planewaves are forbidden, only regions of the Brillouin zone (BZ) near these lifted degeneracies contribute to optical properties. Application to optical response of Si and other semiconductors reveals that a single band transition, with only two planewaves, well describes their dielectric properties. Further, it provides a framework to understand non-linear optical response which is demonstrated to arise from higher order degeneracy existing along high symmetry lines/points of the BZ.

Optical properties are fundamental for many materials applications [1–3], yet they are complex and involve transition dipole matrix elements between different states  $\langle \psi_{n,\mathbf{k}} | \mathbf{r} | \psi_{n',\mathbf{k}} \rangle$  which span the energy spectrum and are over the entire Brillouin zone (BZ). Although first-principles methods can directly calculate these matrix elements [4–7], the complexity makes it challenging to reveal the underlying physics which control these properties. Much of the current understanding is still based on the joint density of states [8–10], wherein the matrix elements are set to unity.

Beyond dipole matrix elements, any perturbative treatment of the system will involve transition matrix elements between state, which broadly affect the material characteristics, e.g., dielectric screening [11, 12], radiative [13, 14] and non-radiative recombination [15, 16], free-carrier absorption [17], electron-phonon coupling [18], and therefore carrier scattering [19]. In the many-body GW quasiparticle calculations, the difficult to converge Coulomb hole involves matrix elements of the form  $\langle \psi_{n,\mathbf{k}} | e^{i(\mathbf{q}+\mathbf{G})\cdot\mathbf{r}} | \psi_{n',\mathbf{k}-\mathbf{q}} \rangle$  where  $n'$  runs over unoccupied states [20].

To develop physical insight into these matrix elements, and hence poorly understood physical properties such as the nonlinear susceptibility, it is critically important to gain an understanding of the wavefunction structure in Fourier space. In this regard, the simplest framework is to view the solid as a free electron gas (FEG) in the presence of a periodic atomic potential. Here, the Bravais lattice defines the FEG states and crystal symmetry imposes restrictions on non-vanishing Fourier components of the potential  $V(\mathbf{G})$ . This so-called empirical pseudopotential method (EPM) has been shown to provide accurate descriptions of the band structures, deformation potentials and optical properties of bulk materials, alloys and nanostructures [21–24].

In this paper, using Bravais lattice symmetry, we gain physical insight into the wavefunction, enabling simple and accurate analytical understanding of optical response

in non-transition-metal solids. A key realization is that all optical transitions of the FEG are *dark*. Hence, only transitions between states which contain common Fourier components can be optically active. Such mixing is most prominent when the potential of the solid breaks the degeneracy of the FEG, defined by the Bravais lattice. Taking Si as a prototype, we show that only the states derived from doubly degenerate FEG states within symmetry planes in BZ dominate the linear optical response. By considering only two planewaves (2G-model), we construct an analytic expression of the transition matrix elements containing only a single coupling parameter determined from first principles.  $\chi^{(1)}$  predicted from this model agrees well with first-principles results and the deviations are well understood by considering higher order degeneracy along symmetry lines. Further, it is precisely these lines of higher order degeneracy which give rise to non-linear optical response. This is demonstrated for GaAs, where contributions from the vicinity of the  $\Gamma$ - $L$  lines dominate  $\chi^{(2)}(\hbar\omega)$ . This is a substantial advance in the current understanding of non-linear optics which largely neglects the transition matrix element, focusing on the joint density of states.

As a starting point for understanding the wavefunction structure in the BZ, we investigated the 1D Kronig-Penney (KP) model [25] for a periodic Dirac potential  $V(x) = \alpha\delta(x - nL)$ , where  $\alpha$  is the potential strength and  $L$  is the periodicity. The KP model can be solved analytically in Fourier space as detailed in 'KP model' section in SI. The band structures of the FEG and KP models are shown in Fig. 1(a), in gray and color, respectively. The FEG eigenstates are planewaves and the corresponding band structure is a folded parabola, leading to double degeneracies at the symmetrical points, i.e.,  $\Gamma$  and  $\pm X$ . After applying the potential  $V(x)$ , these degenerate states are split, opening up band gaps. Away from these  $k$ -points, however, the bands quickly reduce to the FEG band structure of single planewaves. This is seen by examining the KP wavefunctions in the Fourier

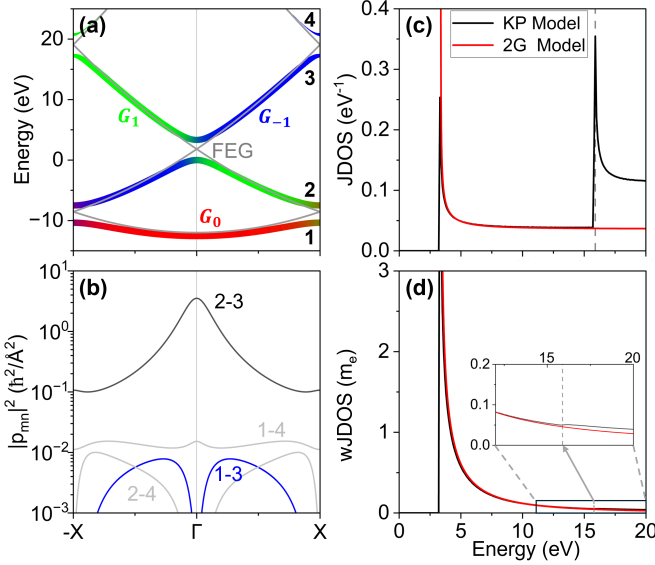


FIG. 1. (a) Shows the energy dispersion, in which we assume the first two bands are fully occupied, while all others are fully empty in line with later discussion for Si. The average potential for FEG and KP model is aligned. The VBM is set to 0 eV. (b) Shows the momentum matrix element squared. (c) Shows the joint density of states (JDOS), and (d) shows  $|p_{mn,k}|^2$  weighted JDOS (wJDOS).

space.

$$\psi_{n,k}(x) = \sum_{G_i} C_{n,k}(G_i) e^{i(k+G_i)x} \quad (1)$$

where  $G_i$  is the reciprocal space vector. The projection of each band onto the  $i^{\text{th}}$  plane wave,  $|C_{n,k}(G_i)|^2$ , is shown by the color in Fig. 1(a). Here it can be seen that the potential causes an anticrossing, leading to a 50% mixture of two plane waves at the high symmetry points. However, moving away from these points, they quickly regain their single plane wave character, with a projection exceeding 94%.

To investigate the optical properties, we examine the dipole transition matrix ( $r_{mn,k}$ ), which for solids is determined from the momentum matrix element [7, 26, 27],

$$p_{mn,k} = \hbar \sum_{G_i} C_{m,k}^*(G_i) C_{n,k}(G_i) G_i, \quad (2)$$

from  $r_{mn,k} = \frac{i\hbar}{m_e} \frac{p_{mn,k}}{E_{n,k} - E_{m,k}}$ . As plane waves are eigenfunctions of the momentum operator, for the FEG,  $p_{mn,k}$  vanishes for all  $m \neq n$ , indicating all transitions are forbidden. According to Eq. (2),  $p_{mn,k}$  can only be nonzero if states  $m$  and  $n$  share at least one common plane wave,  $G_i$ . Therefore, for the KP model, the strength of dipole transition measured by  $|p_{mn,k}|^2$  is negligibly small, except near symmetry points of the BZ. For example, only the transitions between the 2<sup>nd</sup> and 3<sup>rd</sup> band near  $\Gamma$  in Fig. 1(b) have substantial  $|p_{mn,k}|^2$ . This suggests that

the optical properties can be understood simply in terms of the two plane waves,  $G_1$  and  $G_{-1}$ , associated with this transition. Further, it highlights the importance of the transition matrix elements whose information is lacking in the joint density of states (JDOS), Fig. 1(c), which simply measures the density of transitions in an energy window.

To incorporate the strength of these transitions, here we introduce the transition matrix element weighted joint density of states ( $wJDOS$ ) shown in Fig. 1(d),

$$\begin{aligned} wJDOS(E) &= \sum_k \sum_{m,n} \delta(E_{m,k} - E_{n,k} - E) |p_{mn,k}|^2 \\ &= \sum_k f(E, \mathbf{k}) \end{aligned} \quad (3)$$

where the integral of  $wJDOS(E)E^{-1}(E^2 - \hbar^2\omega^2)^{-1}$  is directly proportional to the susceptibility,  $\chi^{(1)}(\hbar\omega)$ . For KP, the most striking difference between the JDOS and  $wJDOS$  seen in Fig. 1 is that the prominent second peak near 15eV in the JDOS has been drastically reduced in the  $wJDOS$ , seen as in the inset in Fig. 1(d). This indeed indicates that  $\chi^{(1)}$  can be understood simply from the primary peak associated with the transition between the 2<sup>nd</sup> and 3<sup>rd</sup> bands. To understand this  $wJDOS$ , we construct a simple two band Hamiltonian (describing the 2<sup>nd</sup> and 3<sup>rd</sup> bands) constructed from the two plane waves  $G_1$  and  $G_{-1}$ , where the coupling is half the bandgap.

$$H = \begin{pmatrix} \frac{\hbar^2}{2m_e} (k + G_1)^2 & \frac{E_g}{2} \\ \frac{E_g}{2} & \frac{\hbar^2}{2m_e} (k + G_{-1})^2 \end{pmatrix}. \quad (4)$$

The results of this 2G-model are shown in red curves in Figs. 1(c) and (d) (see "2G-model" section in SI for the formalism). While the second peak in the JDOS is not represented in this model, we can see the  $wJDOS$  (and hence  $\chi$ ) is very well represented over the entire energy range.

From the EPM perspective, the electronic states of real semiconductors can be understood as a set of plane waves that are coupled by a periodic potential which is expressed as a Fourier series

$$V(\mathbf{r}) = \sum_{\mathbf{G}_s} V_{\mathbf{G}_s} e^{i\mathbf{G}_s \cdot \mathbf{r}}, \quad (5)$$

where,  $V_{\mathbf{G}_s}$  describes the direct coupling between two plane waves whose  $G$ -vectors differ by  $\mathbf{G}_s$ , which decays rapidly with the increase of  $|\mathbf{G}_s|$ . For example, only 3 leading terms  $V_{|\mathbf{G}_s|=\sqrt{3}, \sqrt{8}, \sqrt{11}}$  are needed to accurately describe the Si band structure [22]. Since the FEG states are also a good reference to understanding real semiconductors, the insight of wavefunction structure in Fourier space obtained from 1D model can be naturally extended to real semiconductors. In Fig. 2, we compare the FEG

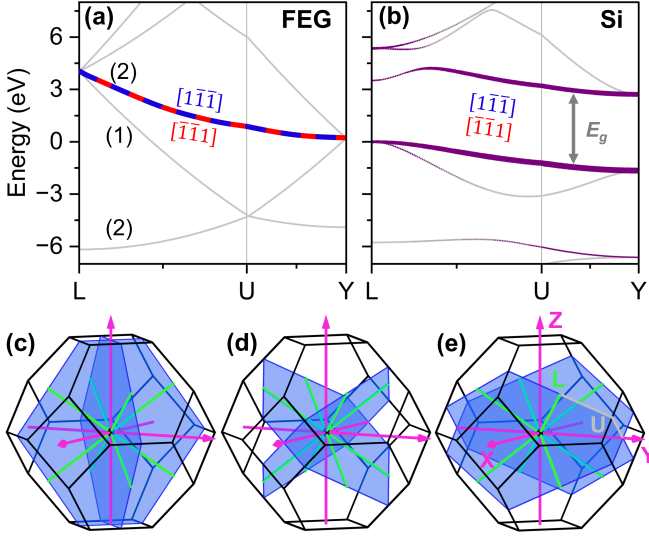


FIG. 2. The band structure of (a) FEG and (b) Si with the wavefunction projection on Fourier component  $[1\bar{1}\bar{1}]$  (blue) and  $[\bar{1}\bar{1}1]$  (red). In panel (b) the purple color indicates the uniform mixing between these two components. (c-e) sketches the  $\sqrt{8}$ -planes, which are (c)  $k_x = \pm k_y$  (d)  $k_y = \pm k_z$  and (e)  $k_z = \pm k_x$

band structure to that of Si calculated using DFT. Surprisingly, these band structures look quite similar, and the details of the Si band structure can be primarily understood from the splitting of degeneracies in the FEG. A key distinction from the 1D case is that in 3D the degeneracy of the FEG is not limited to high symmetry points, but states can also be degenerate along high-symmetry lines or within planes of the BZ. Indeed, along the  $L \rightarrow U \rightarrow Y$  path shown in Fig. 2, the  $\mathbf{G}_{n1} = [1\bar{1}\bar{1}]$  and  $\mathbf{G}_{n2} = [\bar{1}\bar{1}1]$  planewaves are degenerate for the FEG. However, for Si, in addition to the splitting seen at high symmetry points, e.g. L and U, this doubly degenerate band splits, leading to the opening of the gap between occupied and unoccupied states which is responsible for the semiconducting nature of Si.

The splitting of this doubly degenerate band can be understood from the EPM description of Si, in which the  $\sqrt{8}$  term of the potential directly couples  $\mathbf{G}_{n1}$  and  $\mathbf{G}_{n2}$ , as  $|\mathbf{G}_{n1} - \mathbf{G}_{n2}| = \sqrt{8}$ . As the gap originates from this splitting, the highest valence band and lowest conduction band have Fourier component projections, Fig. 2(b), containing approximately equal weights of  $\mathbf{G}_{n1}$  and  $\mathbf{G}_{n2}$ , similar to the mixing observed at  $\Gamma$  in Fig. 1(a). This is especially important in an optical context, as it is the states, which arise from such splitting, have substantial strength of dipole transition.

To understand the optical properties, we focus on such states derived from doubly degenerate ( $n=2$ ) FEG states, dominated by two Fourier components (i.e.,  $\mathbf{G}_{n1}$  and  $\mathbf{G}_{n2}$ ), as these FEG states are degenerate along an entire plane in the BZ, and hence have the largest weight.

There are three conditions that must be simultaneously satisfied for such states: (1) the degeneracy implies

$$(\mathbf{k} + \mathbf{G}_{n1})^2 = (\mathbf{k} + \mathbf{G}_{n2})^2 \quad (6a)$$

(2) for the degeneracy to split, the Fourier component of the potential must couple the states at  $\mathbf{G}_{n1}$  and  $\mathbf{G}_{n2}$ . For Si, this means:

$$|\mathbf{G}_{n1} - \mathbf{G}_{n2}| = \sqrt{3}, \sqrt{8}, \text{ or } \sqrt{11} \quad (6b)$$

(3) For linear optical response, only the dipole transitions from occupied to unoccupied states affect the properties, as such the split degeneracy must straddle the band gap. The doubly degenerate FEG states that satisfies all these requirements are listed in Tab. S1 in SI, which shares the common features of  $|\mathbf{G}_{n1} - \mathbf{G}_{n2}| = \sqrt{8}$  and  $|\mathbf{G}_{n1}| = |\mathbf{G}_{n2}|$ . For these FEG states, the set of  $\mathbf{k}$  points satisfying Eq. (6a) forms 6 planes, denoted the  $\sqrt{8}$ -planes, in the first BZ, which are  $k_x = \pm k_y$  in Fig. 2 (c),  $k_y = \pm k_z$  in Fig. 2(d) and  $k_z = \pm k_x$  in Fig. 2(e).

After coupling, the FEG states (planewaves) mix to form Si states. Within these  $\sqrt{8}$ -planes, the splitting of the double degeneracy leads to states where  $\mathbf{G}_{n1}$  and  $\mathbf{G}_{n2}$  have equal weights. Using the same simple model presented in Eq. (4) (see "2G-model in 3D" section of the SI for details),

$$|(\mathbf{p}_{mn,\mathbf{k}})_z|^2 = \hbar^2 \frac{A^2 (\mathbf{G}_{n1} - \mathbf{G}_{n2})_z^2}{E^2} \quad (7a)$$

$$E(\mathbf{k}) = \sqrt{\left(\frac{\hbar^2}{2m_e}\right)^2 (\mathbf{k} \cdot \hat{\mathbf{n}})^2 |\mathbf{G}_{n1} - \mathbf{G}_{n2}|^2 + 4A^2}, \quad (7b)$$

where  $E$  the energy difference after splitting,  $A$  is the coupling constant and  $\hat{\mathbf{n}}$  is the normal vector of the  $\sqrt{8}$ -plane. When moving away from the plane, the energy difference increases while the strength of dipole transition decreases. Focusing on light polarized in the  $z$ -direction, from Eqs. (7a) and (7b),

$$wJDOS_{\hat{z}} = 8m_e \frac{A^2}{E^2} \sqrt{\frac{E^2}{E^2 - 4A^2}}, \quad (8)$$

where the  $\hat{z}$  indicates that the JDOS is weighted by  $|(\mathbf{p}_{mn,\mathbf{k}})_z|^2$ , and the coupling constant  $A$  is determined from the energy splitting of the states in DFT ( $A = E_g/2$ ), as shown in Fig. 2(b). Similar to the KP model in 1D, here we see that the 2G-model faithfully represents the major peak and tail of the 3D  $wJDOS_{\hat{z}}$  of Si determined by DFT in Fig. 3(a).

To gain further insight,  $f(E, \mathbf{k})$ , defined in Eq. (3), is integrated over the energy windows labeled b, c, d and e in Fig. 3(a) and shown in Figs. 3(b-e) for DFT and in Figs. 3(b'-e') for the 2G-model. While (b) and (b') show a substantial difference, both Figs. 3(c) and

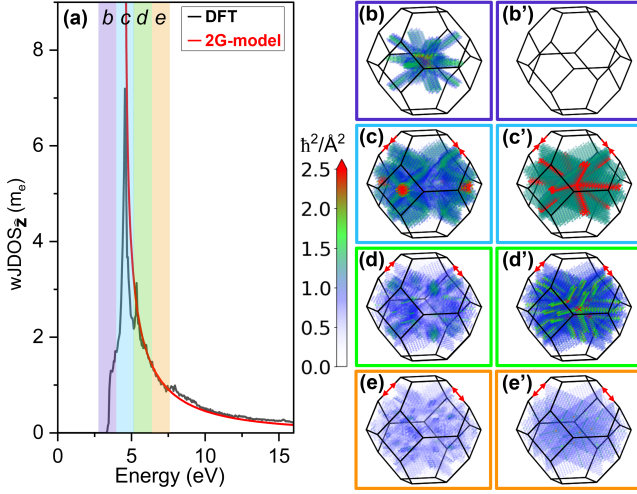


FIG. 3. (a) shows the  $wJDOS_z$  of bulk Si from DFT calculation (black) and 2G-model (red). (b-e) and (b'-e') show the integral of  $f(E, \mathbf{k})$  in Eq. (3) over  $E$  within each energy window indicated in (a) for each  $\mathbf{k}$  point from (b-e) DFT calculation and 2G-model (b'-e').

(c') can be seen to have the major contribution from the four  $\sqrt{8}$ -planes associated with  $(\mathbf{p}_{mn,k})_z$ . Here it can be seen that it is indeed these planes which give rise to the major peak in the  $wJDOS_z$ , seen in energy window c. As the energy window is shifted to higher energies, this corresponds to a larger energy separation between states in the 2G-model (Eq. (7b)) which is associated with increasing the distance  $(\mathbf{k} \cdot \hat{n})$  from the  $\sqrt{8}$ -planes. As a result, Figs. 3(d) and (d') reveal that the major contributions originate from pairs of planes parallel to but offset from the  $\sqrt{8}$  planes. As the energy further increases, the spacing between these planes grows and the magnitude of the matrix elements diminishes as shown in Figs 3 (e) and (e').

As the 2G-model captures the essential physics of the splitting of the two-fold planar degeneracy, the major peak and tail of the  $wJDOS_z$  are well represented. Further, in the  $\hbar\omega \rightarrow 0$  limit, it captures nearly 90% of the contribution to linear optical susceptibility as depicted in Fig. 4. While the 2G-model focuses on degenerate planes, we note that at the intersection of these planes, we have lines of higher degeneracy involving more than two planewaves. The affect of neglecting these higher order degeneracies can be seen in Fig. 3(a), where a small shoulder in energy window b and a small secondary peak in energy window d. As detailed in Fig. S2 in SI, spatial decomposition of the  $wJDOS_z$  clearly shows that the region of the BZ near the  $\Gamma$  to  $L$  lines are responsible for both the shoulder and secondary peak while the  $wJDOS_z$  of the other region are accurately captured by the 2G-model. To describe the higher order degeneracy along symmetry lines requires an nG model with  $n > 2$ . A 6G-model effectively captures the key features of these

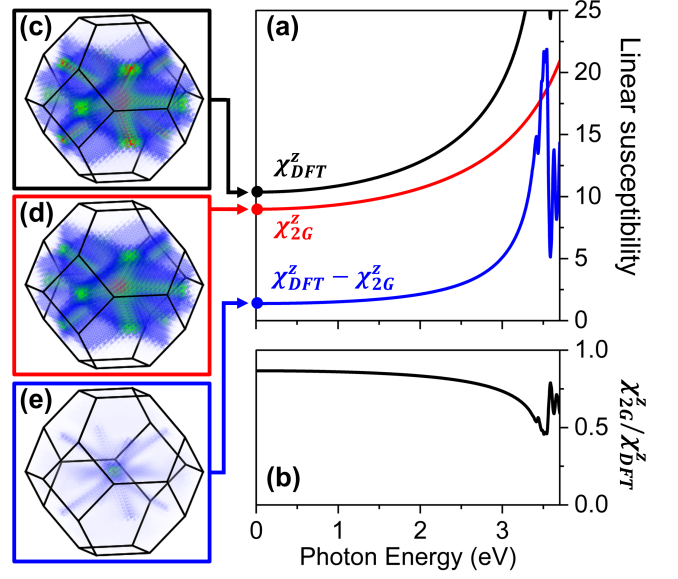


FIG. 4. (a) shows the real part of frequency dependent z component of total susceptibility  $\chi_{DFT}^z(\omega)$  determined from DFT (black) the  $\chi_{2G}^z(\omega)$  determined from the 2G-model (red) and their difference (blue). (b) shows the ratio between  $\chi_{2G}^z(\omega)$  and  $\chi_{DFT}^z(\omega)$ . (c-d) show that k-resolved susceptibility of (c)  $\chi_{DFT}^z(0, \mathbf{k})$ , (d)  $\chi_{2G}^z(0, \mathbf{k})$  and (e) their difference.

higher order contributions to Si, III-V, and II-VI semiconductors, as detailed in the SI.

While such higher order degeneracies have little effect on the linear optical properties, second order harmonics are exclusively determined by the product of matrix elements  $\mathbf{p}_{mn}\mathbf{p}_{nl}\mathbf{p}_{lm}$  where m,n, and l are distinct bands. As such, higher order degeneracy becomes paramount as only states which originate from at least a triple degeneracy have substantial contribution to the non-linear optical response. This is apparent for GaAs shown in Fig. 6. From the inset, it can be seen that contributions to  $\chi^{(2)}$  are dominated by the  $\Gamma$ -L lines, where degenerate FEG planes intersect to form higher order degeneracy. Further, we see that  $\chi^{(2)}$  is well represented over the entire energy range by considering only the region of the BZ near the  $\Gamma$ -L lines.

The key finding of this work is that to a large extent, the wavefunctions of non-transition-metal solids are the same as the FEG, and as such can be represented by a single planewave in most of the BZ. Only in the vicinity of high symmetry areas of the BZ, where the symmetry of the Bravais lattice results in degenerate FEG states, do the wavefunctions of solids have a handful of planewave components. This allows for great simplification of the underlying physics and enables analytical study. Applied to the linear optical response of Si, we find that a single band transition captures the essential physics (nearly 90% of  $\chi^{(1)}$ ). A similar percentage of the non-linear response for GaAs is found to arise from the higher order degeneracies along the  $\Gamma$ -L line. The reduced dimensionality, center



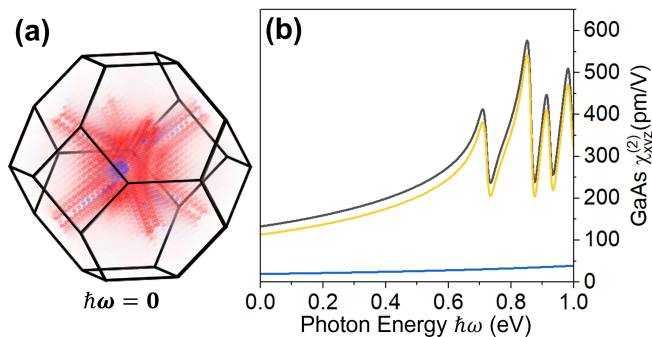


FIG. 5. The calculated non-linear optical response  $\chi^{(2)}$  for GaAs. The inset shows the  $k$ -dependent contribution to  $\chi^{(2)}$  at  $\hbar\omega = 0$ . The black line shows  $\chi^{(2)}(\hbar\omega)$ , where contributions arising from the region near  $\Gamma$ - $L$  (within  $0.32 \text{ \AA}^{-1}$ ) are shown in yellow and those from the remainder of the BZ are shown in blue.

to this framework, not only greatly improves the understanding of the solid state, empowering inverse design, but also opens the door to drastically reducing the computational effort associated with manybody calculations.

## METHOD

The first principles calculations are performed via the ABINIT code [28–30] based on Fritz-Haber-Institute (FHI) norm-conserving pseudopotential and Perdew-Burke-Ernzerhof (PBE) functional [31]. For optical and band structure calculations a  $31 \times 31 \times 31$  Monkhorst-Pack  $k$ -point mesh and kinetic energy cutoff of 20 Ha. are applied with the convergence criteria set to  $10^{-10} \text{ Ha}$ . The spin-orbit coupling is not considered. Optical properties are calculated using 12 empty conduction bands and experimental lattice constants [32] for all studied materials (Si, GaAs and ZnSe). To match the calculated band gaps with experimental values [32], scissor corrections of 0.7 eV for Si and GaAs, 1.4 eV for ZnSe are applied.

All the  $k$ -resolved spectrum are obtained in the  $31 \times 31 \times 31$  Monkhorst-Pack  $k$ -point mesh. For the wJDOS from DFT, the  $\delta$  function in Eq. (3) are approximated by dividing the energy range into small energy windows of 0.05 eV width and sum over states within each window. To obtain a smooth curve for JDOS and wJDOS, the Monte Carlo sampling of reciprocal space is applied, where 40000  $k$  points are randomly selected within the first BZ.

## ACKNOWLEDGMENTS

This work was supported by the U.S. DOE Grant No. DE-SC0002623. The supercomputer time sponsored by National Energy Research Scientific Center (NERSC) under DOE Contract No. DE-AC02-05CH11231 and the

Center for Computational Innovations (CCI) at Rensselaer Polytechnic Institute (RPI) are also acknowledged.

- [1] M. L. Cohen and J. R. Chelikowsky, *Electronic structure and optical properties of semiconductors*, Vol. 75 (Springer Science & Business Media, 2012).
- [2] Q. H. Wang, K. Kalantar-Zadeh, A. Kis, J. N. Coleman, and M. S. Strano, *Nature nanotechnology* **7**, 699 (2012).
- [3] S.-P. Guo, Y. Chi, and G.-C. Guo, *Coordination Chemistry Reviews* **335**, 44 (2017).
- [4] R. Nunes and X. Gonze, *Physical Review B* **63**, 155107 (2001).
- [5] I. Souza, J. Íñiguez, and D. Vanderbilt, *Physical review letters* **89**, 117602 (2002).
- [6] M. Gajdoš, K. Hummer, G. Kresse, J. Furthmüller, and F. Bechstedt, *Physical Review B* **73**, 045112 (2006).
- [7] C. Ambrosch-Draxl and J. O. Sofo, *Computer physics communications* **175**, 1 (2006).
- [8] M. Amiotti, A. Borghesi, G. Guizzetti, and F. Nava, *Physical Review B* **42**, 8939 (1990).
- [9] S. K. O’Leary, S. Zukotynski, and J. M. Perz, *Physical Review B* **52**, 7795 (1995).
- [10] S. K. O’Leary, S. Johnson, and P. Lim, *Journal of applied physics* **82**, 3334 (1997).
- [11] C. M. Bertoni, V. Bortolani, C. Calandra, and E. Tosatti, *Physical Review B* **9**, 1710 (1974).
- [12] M. S. Hybertsen and S. G. Louie, *Physical Review B* **35**, 5585 (1987).
- [13] W. P. Dumke, *Physical Review* **105**, 139 (1957).
- [14] A. Dmitriev and A. Oruzhenikov, *Journal of applied physics* **86**, 3241 (1999).
- [15] D. Laks, G. Neumark, and S. Pantelides, *Physical Review B* **42**, 5176 (1990).
- [16] E. Kioupakis, D. Steiauf, P. Rinke, K. T. Delaney, and C. G. Van de Walle, *Physical Review B* **92**, 035207 (2015).
- [17] E. Kioupakis, P. Rinke, A. Schleife, F. Bechstedt, and C. G. Van de Walle, *Physical Review B* **81**, 241201 (2010).
- [18] F. Giustino, *Reviews of Modern Physics* **89**, 015003 (2017).
- [19] F. Murphy-Armando and S. Fahy, *Physical Review B* **78**, 035202 (2008).
- [20] S. Zhang, D. Tománek, M. L. Cohen, S. G. Louie, and M. S. Hybertsen, *Physical Review B* **40**, 3162 (1989).
- [21] P. Friedel, M. Hybertsen, and M. Schlüter, *Physical Review B* **39**, 7974 (1989).
- [22] S. Zhang, C.-Y. Yeh, and A. Zunger, *Physical Review B* **48**, 11204 (1993).
- [23] M. V. Fischetti and S. E. Laux, *Journal of Applied Physics* **80**, 2234 (1996).
- [24] R. Kim and Y.-W. Son, *Physical Review B* **109**, 045153 (2024).
- [25] S. Singh, *American Journal of Physics* **51**, 179 (1983).
- [26] J. Sipe and E. Ghahramani, *Physical Review B* **48**, 11705 (1993).
- [27] S. Sharma and C. Ambrosch-Draxl, *Physica Scripta* **2004**, 128 (2004).
- [28] X. Gonze, J.-M. Beuken, R. Caracas, F. Detraux, M. Fuchs, G.-M. Rignanese, L. Sindic, M. Verstraete,

- G. Zerah, F. Jollet, *et al.*, Computational Materials Science **25**, 478 (2002).
- [29] X. Gonze, B. Amadon, P.-M. Anglade, J.-M. Beuken, F. Bottin, P. Boulanger, F. Bruneval, D. Caliste, R. Caracas, M. Côté, *et al.*, Computer Physics Communications **180**, 2582 (2009).
- [30] X. Gonze, B. Amadon, G. Antonius, F. Arnardi, L. Baguet, J.-M. Beuken, J. Bieder, F. Bottin, J. Bouchet, E. Bousquet, *et al.*, Computer Physics Communications **248**, 107042 (2020).
- [31] J. P. Perdew, K. Burke, and M. Ernzerhof, Physical review letters **77**, 3865 (1996).
- [32] O. Madelung, *Semiconductors: data handbook* (Springer Science & Business Media, 2004).